

Lead-Free Perovskite Nanowire Array Photodetectors with Drastically Improved Stability in Nanoengineering Templates

Aashir Waleed,[†] Mohammad Mahdi Tavakoli,^{†,‡} Leilei Gu,[†] Ziyi Wang,[§] Daquan Zhang,[†] Arumugam Manikandan,[⊥] Qianpeng Zhang,[†] Rongjun Zhang,[§] Yu-Lun Chueh,[⊥] and Zhiyong Fan^{*,†}

[†]Department of Electronic and Computer Engineering, The Hong Kong University of Science and Technology, Clear Water Bay, Kowloon, Hong Kong SAR, China

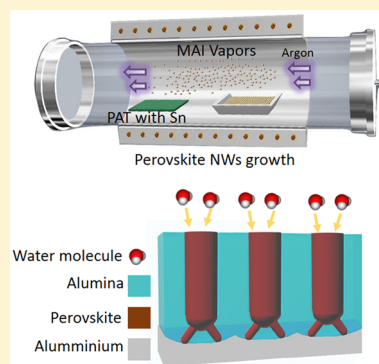
[‡]Department of Materials Science and Engineering, Sharif University of Technology, Azadi Avenue, 113659466 Tehran, Iran

[§]Department of Optical Science and Engineering, Fudan University, Shanghai 200433, China

[⊥]Department of Materials Science and Engineering, National Tsing Hua University, Hsinchu 30013, Taiwan ROC

S Supporting Information

ABSTRACT: Organometal halide perovskite materials have triggered enormous attention for a wide range of high-performance optoelectronic devices. However, their stability and toxicity are major bottleneck challenges for practical applications. Substituting toxic heavy metal, that is, lead (Pb), with other environmentally benign elements, for example, tin (Sn), could be a potential solution to address the toxicity issue. Nevertheless, even worse stability of Sn-based perovskite material than Pb-based perovskite poses a great challenge for further device fabrication. In this work, for the first time, three-dimensional $\text{CH}_3\text{NH}_3\text{SnI}_3$ perovskite nanowire arrays were fabricated in nanoengineering templates, which can address nanowire integration and stability issues at the same time. Also, nanowire photodetectors have been fabricated and characterized. Intriguingly, it was discovered that as the nanowires are embedded in mechanically and chemically robust templates, the material decay process has been dramatically slowed down by up to 840 times, as compared with a planar thin film. This significant improvement on stability can be attributed to the effective blockage of diffusion of water and oxygen molecules within the templates. These results clearly demonstrate a new and alternative strategy to address the stability issue of perovskite materials, which is the major roadblock for high-performance optoelectronics.



KEYWORDS: Organometal perovskite material, nanowire, stability, porous alumina template, photodetector

Organometal halide perovskite materials are promising candidates for high performance optoelectronic devices due to their highly attractive optical and electrical properties such as excellent optical absorption and luminescence efficiency, high carrier mobility, and long carrier diffusion length.^{1–4} Combined with the enticing tunability on composition and material physical properties, these materials have opened up a great deal of opportunities for next generation high performance solar cells, photodetectors, and light-emitting diodes in a broad range of applications from energy conservation to communication. Despite the stunning progress that has been made on high performance device fabrication with the perovskite materials, their toxicity and environmental stability have cast a gloomy shadow over their application potency. Primarily, toxicity originates from utilization of lead (Pb) heavy metal for many organometal halide perovskite materials, such as $\text{CH}_3\text{NH}_3\text{PbI}_3$, $\text{CH}_3\text{NH}_3\text{PbBr}_3$, CsPbI_3 , etc. Substituting Pb with Tin (Sn) could be a potential solution to address the toxicity issue. Nevertheless, even worse stability of Sn based perovskite materials than Pb based perovskites under ambient conditions poses a greater challenge for even material characterization and

device fabrication.^{5,6} Among several factors that trigger perovskite material instability, oxygen and moisture are the primary causes leading to material decomposition and degradation.^{7,8} Significant effort has been exerted on addressing stability issues of perovskite materials via various strategies such as material compositional tuning,^{9,10} crystal structure modification,^{11,12} encapsulation, etc.^{13,14} In fact, encapsulation is of critical importance for all electronic and optoelectronic devices regardless of materials. However, as the vast majority of perovskite material based devices have a planar structure with the active perovskite material sandwiched between two parallel charge transporting layers or electrodes, lateral diffusion of oxygen and water in the active layer cannot be inhibited even with well-designed encapsulation on top of the device; thus, fast material decomposition and device degradation can still occur.^{15,16} It is worth noting that perovskite material decomposition is a self-accelerating process.¹⁷ Specifically, oxygen and water molecules together can directly affect

Received: November 2, 2016

Revised: December 19, 2016

Published: December 23, 2016

perovskite material stability. Water molecules trigger decomposition of $\text{CH}_3\text{NH}_3\text{PbI}_3$, which leads to production of HI.¹⁸ HI reacts with oxygen to form water molecules again to trigger more decomposition in vicinity. This indicates that once a perovskite crystal grain starts to decompose, the decomposition will propagate throughout the entire perovskite film with the presence of oxygen and moisture. This process can be very fast considering the fast diffusion of oxygen and water molecules along grain boundaries of a polycrystalline perovskite film.^{19,20} Therefore, inhibiting oxygen and water molecules lateral diffusion is of paramount importance to improve device stability; nonetheless, it cannot be easily tackled with conventional planar device structure design.

In this work, we demonstrate a unique approach to fabricate $\text{CH}_3\text{NH}_3\text{SnI}_3$ (MASnI_3) nanowires (NWs) for the first time in a chemically and mechanically robust porous alumina template (PAT) using vapor phase chemical reaction method. With this approach, a three-dimensional array of perovskite NWs with density of $4 \times 10^8/\text{cm}^2$ was grown and tightly embedded in PAT; thus, lateral diffusion path of oxygen and water molecules is effectively blocked by alumina sidewalls, which leads to dramatically improved material stability. Specifically, photoluminescence (PL) measurements showed that material degradation process in PAT has been slowed down by ~ 800 times as compared with a planar control sample under regular ambient condition. Meanwhile, NWs and a planar MASnI_3 film have been fabricated into photodetectors for comparison. It was also found that the decay of the light current is ~ 500 -times slower for the NWs device as compared with the planar control device. Successful fabrication of high density three-dimensional perovskite NWs can enable future applications of these promising materials for integrated electronics and optoelectronics. More importantly, utilization of nanoengineering templates for significant material stability improvement presented here demonstrates a new and viable strategy to address the stability issue of perovskite materials, which is the major roadblock for their practical applications for high-performance devices.

The overall growth process for MASnI_3 NWs in a PAT is schematically shown in Figure 1a–d, which consists of several consecutive steps detailed in the Supporting Information.

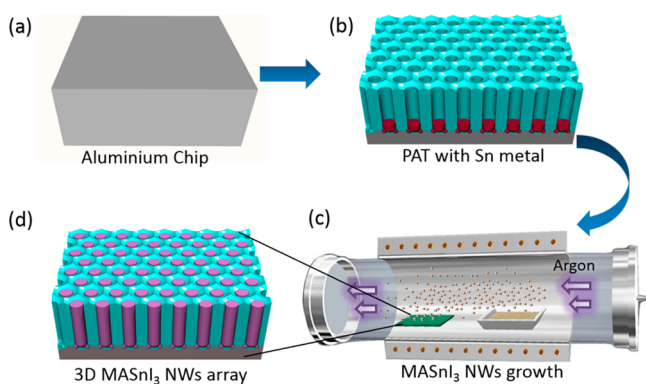


Figure 1. (a) Aluminum chip after electropolishing. (b) Anodized Al chip to form a PAT with well-defined nanopore size and pitch. Then nanoclusters of metal Sn are electrochemically deposited at the bottom of nanopores. (c) Growth schematic for tin perovskite nanowire by vapor diffusion of MAI. The PAT sample is placed next to MAI powder in a tube furnace to carry out MASnI_3 NWs growth at $170\text{ }^\circ\text{C}$. (d) PAT after growth of 3D MASnI_3 NWs.

Briefly, an Al foil is electrochemically polished (Figure 1a) and anodized to form a PAT with well-defined nanopore size and pitch. Then nanoclusters of metal Sn are electrochemically deposited at the bottom of nanopores as one of the precursor material for the subsequent nanowire growth (Figure 1b). Thereafter, the sample is placed next to methylammonium iodide (MAI) powder in a tube furnace to carry out MASnI_3 NWs growth at $170\text{ }^\circ\text{C}$, as shown in Figure 1c and d. In this growth process, MAI vapor is transported to the PAT by the Ar carrier gas and then reacts with the Sn nanoclusters inside the nanopores of the PAT. Thus, essentially it is a vapor phase NWs growth approach. Note that crystalline organometal halide perovskite materials have been predominantly grown with solution process,^{21–25} and vapor phase perovskite NWs growth starting with metal nanoclusters directly serving as a precursor has rarely been reported. In fact, in the past we have successfully fabricated Ag–tetracyanoquinodimethane (Ag-TCNQ) organometallic NWs using organic TCNQ vapor and Ag metal as the precursors, which inspired the growth of organometal halide NWs using metal precursors,²⁶ although their detailed growth mechanisms differ from each other.

Figure 2a shows the top view scanning electron microscopy (SEM) image of the grown MASnI_3 NWs in a highly ordered PAT. The perfect hexagonal ordering of the nanopores was achieved via electrochemical anodization in conjunction with nanoimprint that has been reported by us before.^{27,28} With this method, the diameter and periodicity of the NWs can be precisely controlled, which is highly attractive for photonic and optoelectronic applications.^{29–31} In this work, the NW diameter is 250 nm with periodicity of 500 nm, as shown in Figure 2a. Figure 2b shows the cross-sectional SEM image of NWs embedded in a PAT obtained with back scattered electron (BSE) mode. This confirms the fact that all NWs have almost identical diameter and height, which demonstrates the excellent controllability of the NW growth approach reported here. It is also worth noting that PATs can be readily grown without nanoimprint. In this case, the nanopores and the resulting MASnI_3 NWs are semiordered, as shown in Supplementary Figure S1. We have performed material stability investigations with this type of samples since NW ordering does not affect the physics and chemistry of stability. To investigate the crystal structure of the grown NWs, both transmission electron microscopy (TEM) and X-ray diffraction (XRD) patterns were achieved on the NWs. The inset of Figure 2c shows a SEM image of NWs grown out of nanopores of PAT. These NWs were harvested onto a copper TEM grid, and Figure 2c and d are the TEM image and selective area electron diffraction (SAED) pattern. Particularly, SAED pattern shows an individual NW is crystalline with cubic crystal structure. XRD patterns in Figure 2e were achieved on an array of MASnI_3 NWs in a PAT, which further confirm that the NWs are crystalline with cubic crystal structure.⁶ These results show that vapor phase growth method leads to formation of highly crystalline organometal halide NWs, akin to the catalytic growth of inorganic NWs in PATs.^{27,28} However, it is notably different that in MASnI_3 NWs growth process, metal Sn serves as one of the reaction precursors instead of a catalyst. From the BSE mode SEM image of Figure 2b, it can be clearly seen that metal Sn stays at the root of the NWs, unlike the catalytic inorganic NW growth in which metal catalysts sit at the top of the NWs.^{27,28} In fact, it is crucial to have catalytic nanoparticle capping NWs to sustain the widely reported vapor–liquid–solid (VLS) inorganic NW growth, especially in the case of

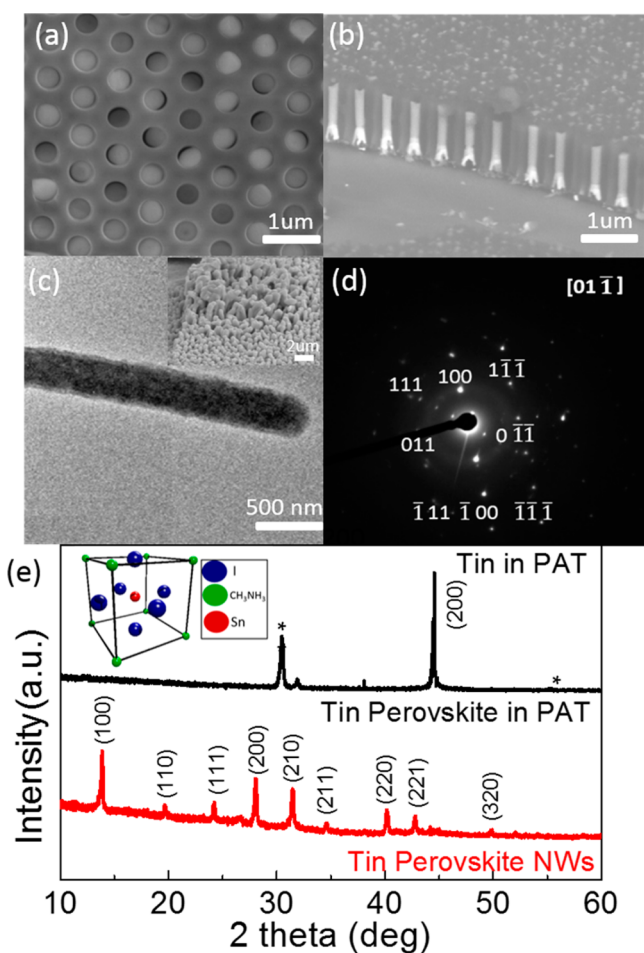


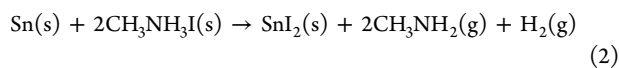
Figure 2. (a) SEM image of tin perovskite nanowires inside PAT (top view). (b) SEM image of tin perovskite nanowires inside PAT (cross-section view). (c) TEM image of a single NW. The inset of panel c shows a SEM image of NWs grown out of nanopores of PAT. These NWs were harvested onto a copper TEM grid for TEM. (d) SAED pattern for tin iodide perovskite nanowire. (e) XRD for tin metal and tin perovskite nanowire inside PAT (insert image shows cubic crystal structure for tin perovskite).

using PATs, since the precursor molecules can only reach the NW/catalyst interface through perpendicular diffusion across the liquid metal catalyst. However, in the case of MASnI_3 , it is apparent that a MAI molecule from free space has to diffuse perpendicularly through a NW to reach Sn/NW interface and thus sustain the continuous reaction and NW growth. Given relatively large lattice constant of organometal halide perovskite materials, ions and molecules can readily migrate and diffuse.^{32,33}

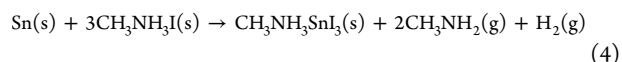
In the past, growth of MASnI_3 predominantly follows the following reaction process if SnI_2 and $\text{CH}_3\text{NH}_3\text{I}$ are used as precursors:



However, in this work, as Sn metal is used as the precursor, a two-step process to form MASnI_3 NWs is described below:



The overall process can be summarized into



In this two-step reaction, SnI_2 is the intermediate product. This reaction process has been confirmed by us in MAPbI_3 NWs growth process recently.³⁴ Since NWs are grown from Sn metal and volumetric expansion from Sn to MASnI_3 is 4.62-times considering the material mass density (Supporting Information), a small amount of Sn can lead to growth of long MASnI_3 NWs.

Upon successful growth of MASnI_3 NW arrays in PATs, their optical properties have been systematically characterized. Since MASnI_3 NWs have not been reported previously, we have also fabricated MASnI_3 thin film samples to compare their optical properties. Supplementary Figure S2a and S2b show the top view and cross-sectional SEM images of a tin perovskite thin film thermally deposited on a FTO glass. As it can be clearly seen, the tin perovskite thin film consists of randomly oriented grains with an average size of 200 nm. This morphology is consistent with previous reports.⁵ Figure 3a shows photoluminescence (PL) measurement result of MASnI_3 NWs demonstrating a sharp excitonic peak, and optical absorbance obtained with ultraviolet–visible (UV–vis) spectroscopy. Note that for UV–vis measurement, a 1 μm thick PAT embedded with MASnI_3 NWs is mounted on a glass substrate with UV curable optical epoxy for transmittance measurement, as shown in the inset of Figure 3a. Clearly, these optical measurements indicate that MASnI_3 NWs have a band gap of 1.3 eV. The PL and UV–vis measurement results for MASnI_3 thin film shown in Supplementary Figure S2c also demonstrate the consistent band gap value, which matches well with existing theoretical and practical values in literature.^{5,6} Together with the TEM and XRD, these data confirm the quality of the grown MASnI_3 NWs.

In addition to PL and absorbance, optical constants including refractive index (n) and extinction coefficient (k) of MASnI_3 NWs have been measured here. Refractive index and extinction coefficient are important optical parameters of a material that can describe how light propagates through the material. To our best knowledge, complex refractive index of MASnI_3 material has never been reported so far. Supplementary Figure S3 shows n and k versus optical wavelength measured with ellipsometry. With measured k , material absorption coefficient α (cm^{-1}) can be calculated using the following formula:

$$\alpha = \frac{4\pi k}{\lambda} \quad (5)$$

Where λ is wavelength in vacuum and centimeter unit. Supplementary Figure S3b shows the calculated absorption coefficient versus wavelength in the range of 200–1000 nm.

The optical measurements have confirmed that MASnI_3 NWs have an optical band gap of 1.3 eV. This suggests that the NWs are highly desirable for many optoelectronic applications including solar cells, photodetectors, etc. The primary advantage of MASnI_3 material compared with the widely researched MAPbI_3 for high performance photovoltaics rests in its nontoxicity by replacing heavy metal Pb with much more environmental friendly Sn. However, chemical and physical stability of MASnI_3 material is even worse than MAPbI_3 , thus limiting its device performance and practical applications. In general, the instability of organometal halide perovskite materials originates from their decomposition upon exposure to water (H_2O) and oxygen (O_2) molecules.^{18,35} By

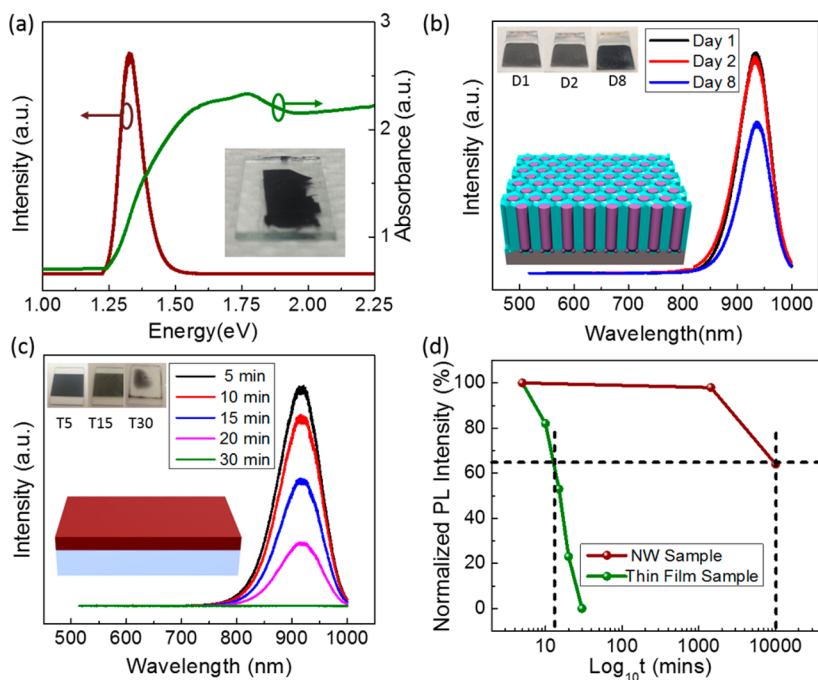


Figure 3. (a) Photoluminescence (PL) emission and absorbance measurement for tin perovskite nanowire inside PAT (inset image is showing free-standing tin perovskite NWs sample for absorbance and PL measurement). (b) PL emission decay measurement for tin perovskite nanowires inside PAT (inset image is showing tin perovskite NWs sample after 1, 2, and 8 days time interval). (c) PL emission decay measurement for tin perovskite thin films (inset image is showing tin perovskite thin film sample after 5, 15, and 30 min time interval). Schematic figures in panels b and c are showing tin perovskite NWs and TF sample, respectively. (d) Normalized PL emission decay from thin film and nanowire samples against logarithmic time scale.

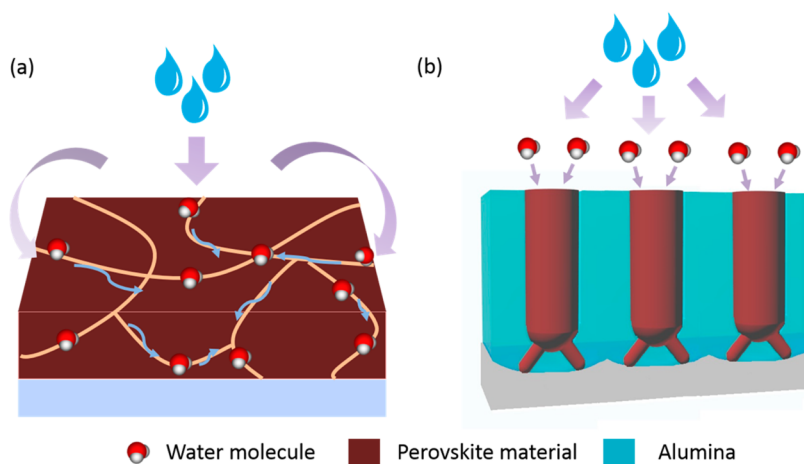
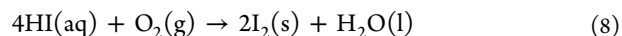
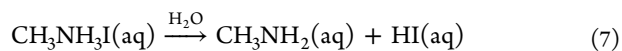


Figure 4. (a) Schematic of tin perovskite thin film decay from moisture. (b) Tin perovskite NWs sample schematic demonstrating sidewall protection of PAT from moisture.

using MAPbI_3 as an example, the degradation process can be formulated as the following:



In this reaction process, consumption of HI, according to reactions 8 and 9, drives the degradation process forward, and production of water in reaction 8 further expedites the

decomposition. Occurrence of material decomposition will certainly degrade the optical and electronic property of the perovskite material. In this work, stability of MASnI_3 NWs has been carefully studied via optical measurements and device characterization. Surprisingly, it was discovered that MASnI_3 NWs have dramatically improved stability over planar MASnI_3 thin films. Specifically, a NWs sample and a thin film after fabrication were kept in air with 70% humidity, and the decay of the materials was monitored by measuring PL peak intensity from time to time. As shown in Figure 3b, PL spectra of as grown MASnI_3 NWs were acquired right after growth (day 1), and after 1 day (day 2), and 7 days (day 8), respectively. It can be seen that in day 2, the PL peak intensity from the NWs

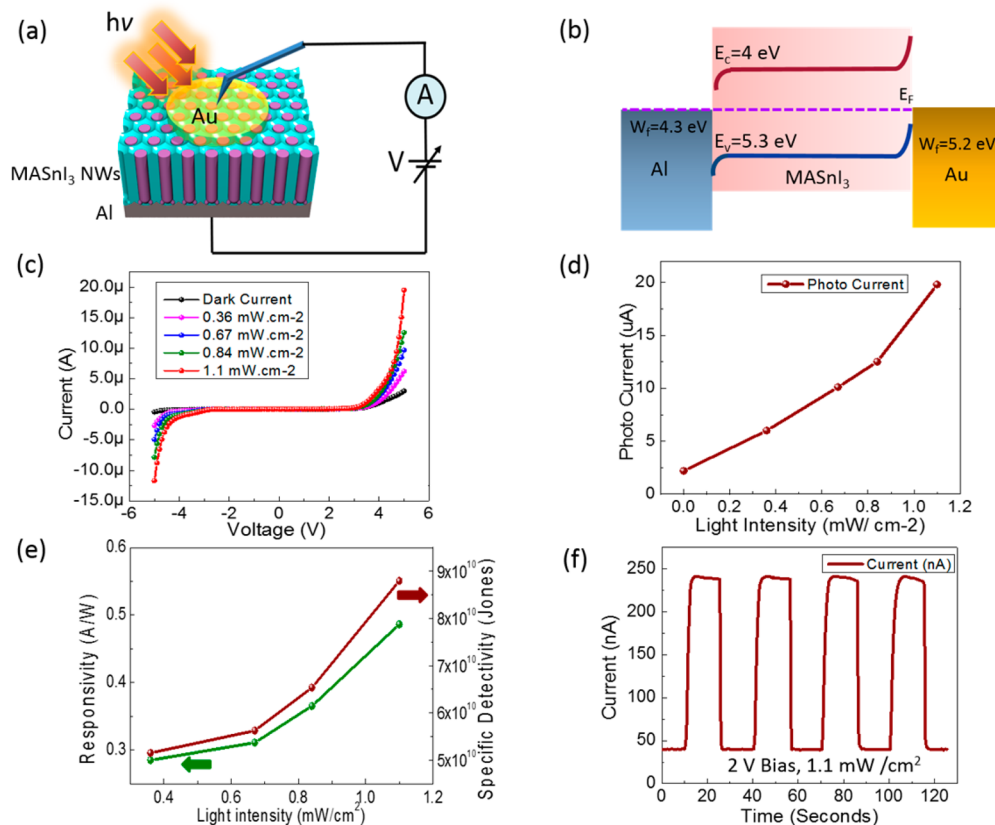


Figure 5. (a) Device schematic for tin perovskite nanowires inside PAT. (b) Band diagram for tin perovskite nanowire device. (c) I - V curves for tin perovskite nanowire device with different light intensities under 5 V bias voltage (-5 V to 5 V sweep range). (d) Photocurrent response of tin perovskite NWs photodetector for different light intensities. (e) Responsivity and specific detectivity of tin perovskite NWs photodetector under different light intensities. (f) I - t curve for tin perovskite NWs photodetector device with light intensity of 1.1 mW/cm² under bias voltage of 2 V.

sample remained almost the same as that in day 1, and the PL intensity at day 8 only degraded to $\sim 65\%$ of that in day 1. The three photos of inset in Figure 3b show the appearance of the sample captured at D1, D2, and D8, which do not demonstrate significant discoloration in the course of the experiment. In contrast, Figure 3c shows the PL peak intensity decay of the control thin film sample. Clearly, fast peak intensity decay is observed, and after 30 min exposure to humid air (70% humidity at 26 °C), the thin film has completely decomposed with disappearance of excitonic emission peak. In fact, this fast decomposition for MASnI₃ thin film is reasonable. In the past, it was well-known that MASnI₃ thin film device fabrication has to be carried out in a glovebox filled with inert gas to retard the degradation process. Figure 3d presents a quantitative analysis of the PL peak intensity decay process for the MASnI₃ NWs and thin film sample. It can be seen that it took 7 days or 10 080 min for the PL peak height of NWs sample to decay down to 65% of its original intensity; however, it only took around 12 min for thin film sample to decay down to the same level. Thus, effectively the decay process of the NWs sample is 840-times slower than that of the thin film sample.

As mentioned above, decomposition of MASnI₃ can be triggered by the reaction between oxygen, water molecules, and the perovskite material. Apart from this, inherent instability of Sn²⁺ ions in the presence of oxygen and moisture is also another cause of quick decay for MASnI₃ as compared to its lead counterpart. Oxygen causes quick oxidation of Sn²⁺ to Sn⁴⁺, which disturbs the overall neutral charge of MASnI₃ and leads to decay of material.⁵ In the polycrystalline thin film

sample as shown in Supplementary Figure S2, there are pinholes and grain boundaries inevitably. Water molecules from atmosphere can easily diffuse through the pinholes and along the grain boundaries to reach each crystalline grain to trigger the decomposition of the thin film in a fast pace.³⁶ Furthermore, once decomposition happens, more pinholes in the thin film are produced, which in turn expedite the decomposition process. This process is schematically demonstrated in Figure 4a. This decomposition process is unavoidable, in principle, increasing grain size and reducing grain boundary area can improve stability. This is consistent with the observation that single crystalline perovskite materials have shown good stability.^{37,38} The fact that MASnI₃ NWs have significantly improved stability is intriguing. It can be rationalized by considering the effective protection provided by PATs. A PAT is mainly composed of alumina, which is electrically insulating, optically transparent, and more importantly, it is a chemically and mechanically robust material. As shown in Figures 1d, and 2a and b, after vapor phase growth, the MASnI₃ NWs are tightly embedded inside the nanopores of the PAT. In this case, the side walls of PAT may block lateral diffusion of water and oxygen molecules inside the NW array; thus, these species can only diffuse vertically from top surface of NWs, resulting in slower decomposition rate. To further study the contribution of PAT to NWs stability, thin-wall PATs with much widened pores were fabricated, as shown in Figure S4a. As seen, the PAT sidewall has gone through significant pore etching; thus, in the red circle regions, the sidewall has been damaged. Sn-based perovskite NWs were grown inside this

PAT, and their stability was evaluated. As shown in Figure S4b, the PL signal intensity at day 8 degraded to $\sim 29\%$ of that in day 1. This degradation rate is obviously much faster than that of the NWs grown in the thick-wall PAT as shown in Figure 3b. Furthermore, PL degradation results from the planar thin film sample, NWs in thick wall PAT, and thin wall PAT are plotted together in Figure S4c, which clearly indicate that although the thin wall PAT could still improve NW stability, it definitely performed worse than the thick wall PAT. This result can be attributed to the thin and damaged sidewall of PAT pores, which cannot block lateral diffusion of oxygen and water molecules as effectively as the thick alumina sidewall. Therefore, these molecules can diffuse faster among adjacent NWs. In addition, unlike in the thin film sample where decomposition self-expedites, NW decomposition may occur vertically due to PAT protection. Therefore, it takes a long time for the entire NW array to decompose. A schematic of the proposed protection mechanism is shown in Figure 4b, in contrast to that occurs in a thin film sample.

It is known that stability of organometal halide perovskite materials can be much improved by proper packaging with polymer materials.⁶ To examine the exterior passivation effect, we packaged NWs and thin film samples with a layer of epoxy (Norland NOA 81) on top of the samples. The PL emission spectra for these samples are provided in Supplementary Figure S5. It can be seen from Figure S5a that the PL peak intensity at day 8 only marginally decreased from day 1 for the NWs sample with epoxy packaging. However, the peak intensity of the thin film sample has decreased down to $\sim 23\%$ at day 8. Furthermore, these samples have been directly placed in deionized water to compare their decomposition rate in an extreme condition. As shown in Supplementary Figure S6, it took 5 days (120 h) for the NWs sample to completely decompose. However, after only 30 h, the thin film sample is completely gone. These results obviously show that proper packaging can indeed largely improve perovskite material stability. Nevertheless, NWs embedded in a PAT have much better stability than a thin film in any condition.

As the perovskite materials have been regarded as highly promising candidates for high performance optoelectronic devices, it is crucial to further verify the stability improvement of MASnI₃ NWs when they are configured as optoelectronic devices. Herein, we have fabricated photodetectors using the grown MASnI₃ NWs, as schematically shown in Figure 5a. In such a device structure, the Al substrate is used as the bottom electrode, and a thin layer of gold (Au) serves as the semitransparent top electrode. Note that as the NWs are vertically well-aligned with ultrahigh density of $4 \times 10^8/\text{cm}^2$, the NW array embedded in PAT can find potential applications for highly integrated electronics and optoelectronics.³⁴ Since different metals are used as contact materials, asymmetric junctions are formed. Figure 5b illustrates the energy band diagram of the device based on the reported work function values of Al (4.3 eV) and Au (5.1 eV) as well as the band structure of MASnI₃ material.⁵ Figure 5c shows the current–voltage (*I*–*V*) characteristics of the device under different halogen lamp light intensity ranging from 0.36–1.1 mW/cm². Clearly, Schottky diode behavior is observed due to asymmetric metal contact. Current increases with increasing light intensity. The energy band diagram of the device in forward bias and reverse bias conditions can be found in Supplementary Figure S7, which can further explain the asymmetric *I*–*V* behavior. Figure 5d demonstrates the photocurrent of the device versus

light intensity acquired under 5 V bias, in which photocurrent can be calculated as

$$\text{Photocurrent } (I_{\text{ph}}) = I_{\text{light}} - I_{\text{dark}} \quad (10)$$

Overall, photocurrent monotonically increases with the intensity of light following a superlinear relationship. Furthermore, responsivity and specific detectivity of the device are calculated and plotted in Figure 5e using the following formula:

$$\text{Responsivity } (R) = \frac{I_{\text{ph}}}{P_{\text{opt}}} \quad (11)$$

$$\text{Specific detectivity} = \frac{R}{(2e \times I_{\text{dark}} \times A^{-1})^{1/2}} \quad (12)$$

In responsivity equation, P_{opt} is the optical power illuminated on the device, which is the product of the intensity of light and the effective device area (0.0314 cm^2). I_{dark} is the device dark current, and A is also the device area. It can be seen that both responsivity and specific detectivity monotonically increase when light intensity increases. The superlinear photocurrent response at higher light intensity is due to relatively high bias voltage and high light intensity.³⁹ Under higher light intensity carrier recombination rate drops, which leads to rise in photocurrent. Recombination rate and light intensity have an inverse relation as explained by Klee, et al. by numerical modeling.³⁹ With 1.1 mW/cm^2 intensity, responsivity can reach up to 0.47 A/W with specific detectivity of 8.80×10^{10} Jones. This high detectivity value is comparable to other lead perovskite based photodetectors.^{40–42} It also suggests that large electrical signals can be generated from small input optical signal. Meanwhile, the responsivity can be further improved if more transparent top electrode is used, such as thinner Au film or ITO film. To examine the response speed of the device, time domain photoresponse of the device was measured with periodically switching halogen light (intensity: 1.1 mW/cm^2) source on and off. Figure 5f shows the recorded dynamic response, and Supplementary Figure S8 shows that the photocurrent has reasonable rise time of 1500 ms and decay time of 400 ms, which can be further improved by reducing length of NWs. Reduction of NWs length causes reduction in NW resistance and consequently carrier transit time.

After systematic characterization of MASnI₃ NWs photodetector, its performance stability is investigated and shown in Figure 6. Specifically, a NWs device and a thin film device without epoxy packaging layer were exposed to air with 70% humidity, and their electrical property was measured from time to time to observe the device degradation. Figure 6a and 6b show the NWs and thin film devices light current decay over time under 5 V bias, respectively. Apparently, it took 7 days for the NWs device light current degrade down to $2.7 \mu\text{A}$ from $19.8 \mu\text{A}$. However, the thin film device completely fails to work with zero light current only 30 min after device fabrication. Figure 6c plots the comparison of the light current decay of the NWs and thin film photodetector. It can be seen that it took around 10 080 min for the NWs device light current to decay down to 14% of its original value; however, it only took ~ 20 min for the thin film device light current to decay down to the same level. Therefore, the decay process of the NWs device is ~ 500 -times slower than that of the thin film device. Supplementary Figure S9 shows photos of the thin film device demonstrating fast material decomposition. It is worth noting

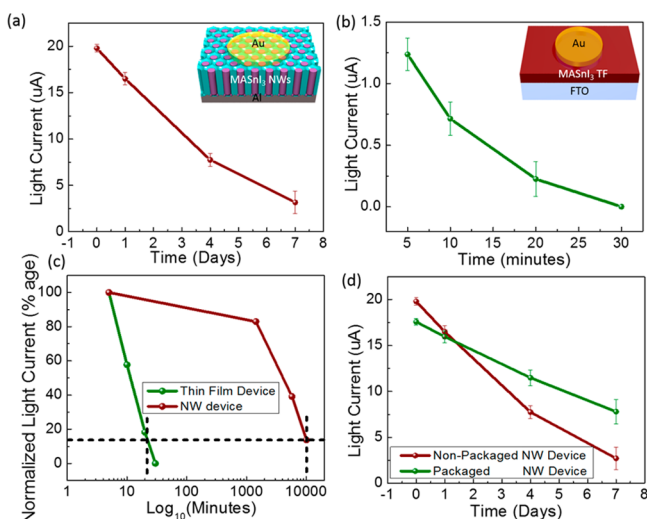


Figure 6. (a) Light current decay for tin perovskite nanowire device inside PAT (insert image is showing NWs based device schematic with circular Au electrode on top). (b) Light current decay for tin perovskite thin film device (insert image is showing thin film device schematic with circular Au electrode on top). (c) Light current decay for packaged and nonpackaged NWs device. (d) Normalized light current decay from thin film and nanowires devices against logarithmic time scale.

that there is a time lag between the thin film fabrication and electrical measurement due to Au electrode deposition on the thin film and the device transfer from evaporator to the measurement set up without using a glovebox; therefore, its measurement starting time is set as 5 min after thin film fabrication. As the thin film has a fast decaying nature, the actual initial light current at “0” min should be much higher than that at 5 min in Figure 6b. This also indicates that the decay slowing down factor of 500 for the NW device is an underestimation since the factor is based on the normalized light current. To investigate the device stability after external packaging, an epoxy passivation layer (Norland NOA 81) was casted on a NW device. As shown in Figure 6d, epoxy packaging indeed can further slow down device degradation. However, as the epoxy curing process requires ultraviolet light soaking for 30 min, it degraded the NW device initial measurement current marginally, as shown in Figure 6d. It was also found that no thin film device can survive this packaging process; thus, no data on thin film device were able to be achieved for comparison.

In this work, we have for the first time fabricated Sn perovskite NWs in PATs with ultrahigh integration density, and the NWs have been fabricated into visible light sensitive photodetector devices with respectable performance. More importantly, stability of NWs and NW devices has been systematically investigated with thin film MASnI_3 as control samples. Intriguingly, it was discovered that the stability of the NWs is close to three orders of magnitude better than that in the thin film control samples. Specifically, PL emission peak intensity decay process is 840-times slower in NWs than in thin films. When NWs and thin films are fabricated into photodetectors, NWs device light current decays 500-times slower than that of the thin film device. The drastic improvement of stability originates from excellent protection provided by the alumina template, which blocks the lateral diffusion of detrimental water and oxygen molecules. Therefore, PATs are

desirable nanoengineering templates to achieve NW integration and improve the material stability at the same time. It is worth mentioning that although MASnI_3 material is explored in this work, which has the most severe stability issue as reported, the conclusion and the NW fabrication scheme can be applied to other organometal perovskite materials. With a broad choice of materials and their properties, the results reported here can potentially enable more practical applications with organometal perovskite materials for high performance electronics and optoelectronics.

■ ASSOCIATED CONTENT

Supporting Information

The Supporting Information is available free of charge on the ACS Publications website at DOI: 10.1021/acs.nanolett.6b04587.

Materials and methods; supporting figures (PDF)

■ AUTHOR INFORMATION

Corresponding Author

*E-mail: eezfan@ust.hk.

ORCID

Aashir Waleed: 0000-0002-6929-8373

Yu-Lun Chueh: 0000-0002-0155-9987

Zhiyong Fan: 0000-0002-5397-0129

Notes

The authors declare no competing financial interest.

■ ACKNOWLEDGMENTS

This work was supported by the General Research Fund (Project Nos. 612113 and 16237816) from the Hong Kong Research Grant Council, the Hong Kong Innovation and Technology Fund (ITS/362/14FP) from the Innovation and Technology Commission. The authors also acknowledge the support from The Center for 1D/2D Quantum Materials and State Key Laboratory on Advanced Displays and Optoelectronics at HKUST.

■ REFERENCES

- (1) Xing, G.; Mathews, N.; Sun, S.; Lim, S. S.; Lam, Y. M.; Gratzel, M.; Mhaisalkar, S.; Sum, T. C. *Science* **2013**, *342*, 344–347.
- (2) Stranks, S. D.; Eperon, G. E.; Grancini, G.; Menelaou, C.; Alcocer, M. J.; Leijtens, T.; Herz, L. M.; Petrozza, A.; Snaith, H. J. *Science* **2013**, *342*, 341–344.
- (3) Nie, W.; Tsai, H.; Asadpour, R.; Blancon, J. C.; Neukirch, A. J.; Gupta, G.; Crochet, J. J.; Chhowalla, M.; Tretiak, S.; Alam, M. A.; Wang, H. L.; Mohite, A. D. *Science* **2015**, *347*, 522–525.
- (4) Dong, Q.; Fang, Y.; Shao, Y.; Mulligan, P.; Qiu, J.; Cao, L.; Huang, J. *Science* **2015**, *347*, 967–970.
- (5) Noel, N. K.; Stranks, S. D.; Abate, A.; Wehrenfennig, C.; Guarnera, S.; Haghighirad, A.-A.; Sadhanala, A.; Eperon, G. E.; Pathak, S. K.; Johnston, M. B.; Petrozza, A.; Herz, L. M.; Snaith, H. J. *Energy Environ. Sci.* **2014**, *7*, 3061–3068.
- (6) Hao, F.; Stoumpos, C. C.; Cao, D. H.; Chang, R. P. H.; Kanatzidis, M. G. *Nat. Photonics* **2014**, *8*, 489–494.
- (7) Aristidou, N.; Sanchez-Molina, I.; Chotchuangchuchaval, T.; Brown, M.; Martinez, L.; Rath, T.; Haque, S. A. *Angew. Chem., Int. Ed.* **2015**, *54*, 8208–8212.
- (8) Zhang, L.; Ju, M.-G.; Liang, W. *Phys. Chem. Chem. Phys.* **2016**, *18*, 23174–23183.
- (9) Tai, Q.; You, P.; Sang, H.; Liu, Z.; Hu, C.; Chan, H. L. W.; Yan, F. *Nat. Commun.* **2016**, *7*, 11105.

- (10) Misra, R. K.; Ciammaruchi, L.; Aharon, S.; Mogilyansky, D.; Etgar, L.; Visoly-Fisher, I.; Katz, E. A. *ChemSusChem* **2016**, *9*, 2572–2577.
- (11) Li, X.; Ibrahim Dar, M.; Yi, C.; Luo, J.; Tschumi, M.; Zakeeruddin, S. M.; Nazeeruddin, M. K.; Han, H.; Grätzel, M. *Nat. Chem.* **2015**, *7*, 703–711.
- (12) Zhang, J.; Xu, B.; Johansson, M. B.; Vlachopoulos, N.; Boschloo, G.; Sun, L.; Johansson, E. M. J.; Hagfeldt, A. *ACS Nano* **2016**, *10*, 6816–6825.
- (13) Liu, Z.; Sun, B.; Shi, T.; Tang, Z.; Liao, G. *J. Mater. Chem. A* **2016**, *4*, 10700–10709.
- (14) Dong, Q.; Liu, F.; Wong, M. K.; Tam, H. W.; Djurišić, A. B.; Ng, A.; Surya, C.; Chan, W. K.; Ng, A. M. C. *ChemSusChem* **2016**, *9*, 2597–2603.
- (15) Han, Y.; Meyer, S.; Dkhissi, Y.; Weber, K.; Pringle, J. M.; Bach, U.; Spiccia, L.; Cheng, Y.-B. *J. Mater. Chem. A* **2015**, *3*, 8139–8147.
- (16) Shoaee, S.; Durrant, J. R. *J. Mater. Chem. C* **2015**, *3*, 10079–10084.
- (17) Cheng, Y.; Yang, Q.-D.; Xiao, J.; Xue, Q.; Li, H.-W.; Guan, Z.; Yip, H.-L.; Tsang, S.-W. *ACS Appl. Mater. Interfaces* **2015**, *7*, 19986–19993.
- (18) Niu, G.; Guo, X.; Wang, L. *J. Mater. Chem. A* **2015**, *3*, 8970–8980.
- (19) Frost, J. M.; Butler, K. T.; Brivio, F.; Hendon, C. H.; van Schilfgaarde, M.; Walsh, A. *Nano Lett.* **2014**, *14*, 2584–2590.
- (20) Manser, J. S.; Saidaminov, M. I.; Christians, J. A.; Bakr, O. M.; Kamat, P. V. *Acc. Chem. Res.* **2016**, *49*, 330–338.
- (21) You, J.; Hong, Z.; Yang, Y.; Chen, Q.; Cai, M.; Song, T.-B.; Chen, C.-C.; Lu, S.; Liu, Y.; Zhou, H.; Yang, Y. *ACS Nano* **2014**, *8*, 1674–1680.
- (22) Adam, G.; Kaltenbrunner, M.; Glowacki, E. D.; Apaydin, D. H.; White, M. S.; Heilbrunner, H.; Tombe, S.; Stadler, P.; Ernecker, B.; Klampfl, C. W.; Sariciftci, N. S.; Scharber, M. C. *Sol. Energy Mater. Sol. Cells* **2016**, *157*, 318–325.
- (23) Eperon, G. E.; Burlakov, V. M.; Docampo, P.; Goriely, A.; Snaith, H. J. *Adv. Funct. Mater.* **2014**, *24* (1), 151–157.
- (24) Yakunin, S.; Sytnyk, M.; Kriegner, D.; Shrestha, S.; Richter, M.; Matt, G. J.; Azimi, H.; Brabec, C. J.; Stangl, J.; Kovalenko, M. V.; Heiss, W. *Nat. Photonics* **2015**, *9*, 444–449.
- (25) Yang, Y.; Yang, M.; Li, Z.; Crisp, R.; Zhu, K.; Beard, M. C. *J. Phys. Chem. Lett.* **2015**, *6*, 4688–4692.
- (26) Fan, Z.; Mo, X.; Lou, C.; Yao, Y.; Wang, D.; Chen, G.; Lu, J. G. *IEEE Trans. Nanotechnol.* **2005**, *4*, 238–241.
- (27) Fan, Z.; Razavi, H.; Do, J.-w.; Moriwaki, A.; Ergen, O.; Chueh, Y.-L.; Leu, P. W.; Ho, J. C.; Takahashi, T.; Reichertz, L. A.; Neale, S.; Yu, K.; Wu, M.; Ager, J. W.; Javey, A. *Nat. Mater.* **2009**, *8*, 648–653.
- (28) Ergen, O.; Ruebusch, D. J.; Fang, H.; Rathore, A. A.; Kapadia, R.; Fan, Z.; Takei, K.; Jamshidi, A.; Wu, M.; Javey, A. *J. Am. Chem. Soc.* **2010**, *132*, 13972–13974.
- (29) Kapadia, R.; Fan, Z.; Javey, A. *Appl. Phys. Lett.* **2010**, *96*, 103116.
- (30) Leung, S.-F.; Yu, M.; Lin, Q.; Kwon, K.; Ching, K.-L.; Gu, L.; Yu, K.; Fan, Z. *Nano Lett.* **2012**, *12*, 3682–3689.
- (31) Haberkorn, N.; Gutmann, J. S.; Theato, P. *ACS Nano* **2009**, *3*, 1415–1422.
- (32) Haruyama, J.; Sodeyama, K.; Han, L.; Tateyama, Y. *J. Am. Chem. Soc.* **2015**, *137*, 10048–10051.
- (33) Azpiroz, J. M.; Mosconi, E.; Bisquert, J.; De Angelis, F. *Energy Environ. Sci.* **2015**, *8*, 2118–2127.
- (34) Gu, L.; Tavakoli, M. M.; Zhang, D.; Zhang, Q.; Waleed, A.; Xiao, Y.; Tsui, K.-H.; Lin, Y.; Liao, L.; Wang, J.; Fan, Z. *Adv. Mater.* **2016**, *28*, 9713.
- (35) Bryant, D.; Aristidou, N.; Pont, S.; Sanchez-Molina, I.; Chotchunangatchaval, T.; Wheeler, S.; Durrant, J. R.; Haque, S. A. *Energy Environ. Sci.* **2016**, *9*, 1655–1660.
- (36) Li, D.; Bretschneider, S. A.; Bergmann, V. W.; Hermes, I. M.; Mars, J.; Klasen, A.; Lu, H.; Tremel, W.; Mezger, M.; Butt, H.-J.; Weber, S. A. L.; Berger, R. *J. Phys. Chem. C* **2016**, *120*, 6363–6368.
- (37) Yen, H.-J.; Liang, P.-W.; Chueh, C.-C.; Yang, Z.; Jen, A. K. Y.; Wang, H.-L. *ACS Appl. Mater. Interfaces* **2016**, *8*, 14513–14520.
- (38) Fu, Y.; Meng, F.; Rowley, M. B.; Thompson, B. J.; Shearer, M. J.; Ma, D.; Hamers, R. J.; Wright, J. C.; Jin, S. *J. Am. Chem. Soc.* **2015**, *137*, 5810–5818.
- (39) Klee, V.; Preciado, E.; Barroso, D.; Nguyen, A. E.; Lee, C.; Erickson, K. J.; Triplett, M.; Davis, B.; Lu, I. H.; Bobek, S.; McKinley, J.; Martinez, J. P.; Mann, J.; Talin, A. A.; Bartels, L.; Léonard, F. *Nano Lett.* **2015**, *15*, 2612–2619.
- (40) Maculan, G.; Sheikh, A. D.; Abdelhady, A. L.; Saidaminov, M. I.; Haque, M. A.; Murali, B.; Alarousu, E.; Mohammed, O. F.; Wu, T.; Bakr, O. M. *J. Phys. Chem. Lett.* **2015**, *6*, 3781–3786.
- (41) Sutherland, B. R.; Johnston, A. K.; Ip, A. H.; Xu, J.; Adinolfi, V.; Kanjanaboos, P.; Sargent, E. H. *ACS Photonics* **2015**, *2*, 1117–1123.
- (42) Kwak, D.-H.; Lim, D.-H.; Ra, H.-S.; Ramasamy, P.; Lee, J.-S. *RSC Adv.* **2016**, *6* (69), 65252–65256.